

Tuning the memristive response of TaO_x- based devices with Ag Nanoparticles

R. Leal Martir^{1,2}, A.J.T. van der Ree^{3,4}, M. H. Aguirre^{5,6,7}, G. Palasantzas^{3,4}, D. Rubi⁸, and M. J. Sánchez^{1,2,*}

¹*Instituto de Nanociencia y Nanotecnología (INN), CONICET-CNEA, nodo Bariloche, 8400 San Carlos de Bariloche, Río Negro, Argentina.*

²*Centro Atómico Bariloche, Instituto Balseiro (UNCuyo), CONICET, 8400 San Carlos de Bariloche, Río Negro, Argentina.*

³*Zernike Institute for Advanced Materials, University of Groningen, 9747 AG Groningen, The Netherlands.*

⁴*CogniGron Center, University of Groningen, 9747 AG Groningen, The Netherlands.*

⁵*Instituto de Nanociencia y Materiales de Aragón (INMA-Unizar), Zaragoza, Spain.*

⁶*Departamento de Física de la Materia Condensada, UNIZAR, Zaragoza, Spain.*

⁷*Laboratorio de Microscopías Avanzadas, UNIZAR-CSIC, Zaragoza, Spain.*

⁸*Laboratorio de Ablación Láser (INN-CONICET-CNEA), Centro Atómico Constituyentes, Gral. Paz 1499, San Martín, Argentina.*

(*maria.sanchez@ib.edu.ar)

Abstract

Defect engineering is a key strategy to control resistive switching (RS) in oxide-based memristive devices, where oxygen vacancy (OV) dynamics governs filament formation and rupture. We investigate the effect of Ag nanoparticles (AgNPs) embedded in the top electrode of Pt/Ta₂O₅/TaO₂/Pt memristors and analyze their RS behavior and statistical stability. Devices without AgNPs exhibit two hysteresis switching loops (HSLs) with opposite chiralities, originating from the participation of the Pt/Ta₂O₅ top interface and the Ta₂O₅/TaO₂ bottom interface. Incorporating AgNPs reduces the overall device resistance and selectively suppresses one loop, yielding a single, well-defined switching mode. Moreover, devices incorporating AgNPs show markedly reduced cycle-to-cycle variability of the high-resistance state, as confirmed by Weibull analysis, indicating improved endurance and switching reproducibility. Within a filamentary RS framework, we attribute this behavior to local metallization of the top interface by AgNPs, which partially inhibit OV transport and confines the RS dynamics to the bottom interface. Numerical simulations with the Oxygen Vacancy Resistive Network (OVRN) model successfully reproduce the experimental HSLs, statistical trends, and tunable ON/OFF ratios with AgNPs coverage. These findings demonstrate that targeted interface metallization via metallic nanoparticles provides an effective route to control multi-interface RS dynamics and improve switching stability in without modifying the oxide architecture.

I. INTRODUCTION

Defect engineering plays a crucial role in the development and optimization of memristive devices, as the presence, distribution, and dynamics of defects critically influence their resistive switching (RS) performance, namely the reversible change in resistance induced by the application of an external electrical stimulus [1, 2]. By carefully tailoring the concentration and spatial arrangement of defects, it is possible to control the formation and rupture of conductive filaments, tune switching thresholds, and improve device performance in terms of speed, endurance, and retention [3–6]. Moreover, defect engineering enables the modulation of non-volatile memory states and enhances the reproducibility of switching processes, which are essential for reliable integration into neuromorphic computing architectures [7–9]. As a result, understanding and manipulating defects at the atomic scale has become a key strategy for advancing memristor technologies toward practical applications.

Within transition-metal-oxide (TMO) memristors, particularly binary oxides such as TiO₂,

VO_2 , HfO_2 , and TaO_2 [10–13], which exhibit a decrease in local resistivity with decreasing oxygen content [14–16], RS is generally attributed either to the migration of oxygen vacancies (OVs) in regions confined to the oxide/electrode interfaces [17–19] or to the formation and rupture of OV filaments spanning the oxide layer [1, 20, 21]. This latter mechanism, known as filamentary resistive switching (FRS), has been extensively investigated using a variety of experimental techniques over the last years [10, 12, 22–27]. Despite its technological promise, FRS remains constrained by reliability challenges, including limited endurance, unstable conductive pathways, and poor data retention.

In multilayer or asymmetric oxide systems, an additional level of complexity arises from the coexistence of multiple (active) interfaces. When two or more interfaces contribute to OV dynamics, distinct switching channels may coexist or compete within the same device, giving rise to multiple hysteresis switching loops (HSLs) with different polarities or chiralities. Such behavior has been reported in TaO_x -based systems, where both oxide/electrode and oxide/oxide interfaces can actively participate in RS [18, 19, 21]. While this multi-interface activity provides additional degrees of freedom for tailoring device functionality, it also increases the number of accessible microscopic switching configurations, often resulting in increased cycle-to-cycle variability and reduced endurance. Strategies capable of selectively activating or suppressing specific switching channels, without modifying the oxide stack itself, remain limited.

Defect engineering has therefore been increasingly explored as a means to stabilize filament dynamics and improve device robustness. Strategies such as incorporating Cu nanoparticles into electrodes [7] or introducing Ag/Cu nanoparticles either within the oxide matrix [28, 29] or at electrode interfaces [30] have demonstrated varying degrees of success in enhancing switching uniformity and reliability. However, in many cases the physical mechanisms by which metallic nanoparticles affect the competition between different OV-driven switching channels remain insufficiently understood.

On the theoretical side, most studies restrict the analysis of defect effects to static electric-field simulations [28–30] or energy band calculations [31, 32], largely because the complex dynamics of OV migration under electrical stress is difficult to capture. The Oxygen Vacancy Resistive Network (OVRN) model [33] overcomes this limitation by explicitly describing (2D) OV dynamics within an array of nanodomains interconnected through a 2D resistor network. This framework enables direct simulations of OV migration and redistribution, naturally incorporates filamentary behavior, and allows the controlled introduction of spatial inhomogeneities, providing a powerful

tool to investigate FRS dynamics in complex oxide systems.

In this work, we introduce Ag nanoparticles (AgNPs) into the top electrode of a Pt/Ta₂O₅/TaO₂/Pt memristive device and investigate their impact on RS. Devices without nanoparticles exhibit two hysteresis switching loops (HSLs) with opposite chiralities—clockwise (CW) and counter-clockwise (CCW)—sharing a common low-resistance state. Upon the incorporation of AgNPs, the overall resistance is reduced and the CCW loop is selectively suppressed, yielding a single, well-defined switching mode.

This behavior can be rationalized within a filamentary RS framework. In devices without AgNPs, Schottky barriers at both the Pt/Ta₂O₅ top interface (TI) [34, 35] and the Ta₂O₅/TaO₂ bottom interface (BI) [18] promote OV migration and enable two competing switching channels. Local metallization of the TI induced by the AgNPs partially inhibits OV transport across this interface, effectively confining the RS dynamics to the BI and suppressing one of the channels. As a result, devices with AgNPs exhibit reduced cycle-to-cycle variability of the high-resistance states, as quantified by Weibull analysis, indicating enhanced switching reproducibility and endurance stability. This physical picture is validated using the OVRN model [33], which reproduces the experimental HSLs and their statistical trends, and shows that the OV dynamics and ON/OFF ratios can be tuned via the AgNPs coverage.

II. METHODS

A bilayer TaO_x thin film was grown over a Si/Pt substrate through Pulsed Laser Deposition (PLD) at room temperature. The lower (35 nm) and upper (15 nm) layers were deposited at oxygen pressures of 0.01 mbar and 0.1 mbar respectively. After the film was grown, AgNPs were deposited on top. This was done through plasma sputtering in a home-modified Mantis Nanogen 50 unit [36, 37]. The coverage (6%) was measured on a simultaneously NP-deposited TEM grid with a Helios G4 scanning electron microscope at 18 kV using HAADF detector. Although other films were fabricated with higher coverages and larger average AgNPs diameters, these conditions are not considered in the present study, as they consistently resulted in device failure. Part of the sample was covered during the deposition, leaving a sector of the film without AgNPs to serve as control. The top Pt electrodes were fabricated using a combination of sputtering and optical lithography. Both regions (those with and without NPs) underwent identical processing, resulting in two types of devices on the same film: one incorporating NPs embedded within the Pt contact,

and one without NPs.

Scanning electron microscopy with high angular annular dark field detector (STEM-HAADF) were performed using a Cs-probe-corrected Titan 360–300 (ThermoFisher) at a working voltage of 300 kV equipped with a EDS detector AZtec from Oxford Instruments with an estimated error in chemical characterization of $\approx 2\%$ [18]. Lamellae were prepared by Focused Ion Beam performed in a Dual Beam Helios NanoLab 650, using a Ga⁺ with acceleration voltage from 5kV up to 30kV. The electrical characterization of the devices was carried out with a Keithley 2636B SMU unit, hooked to a probe station constructed in-house. Device yields were estimated to be approximately 25% and 33% for devices without and with nanoparticles, respectively. The electrical characteristics reported below were reproducibly observed across multiple working devices.

III. EXPERIMENTAL CHARACTERIZATION AND ELECTRICAL RESPONSE

Figure 1a) shows a STEM-HAADF cross-sectional image of a device containing NPs in its pristine (virgin) state. The structure of the TaO_x thin film can be divided into three distinct regions: a top layer (~ 12.5 nm thick, corresponding to Ta₂O₅), a bottom layer (~ 32 nm thick, corresponding to TaO₂), and a transition region between them (~ 3 nm thick). The uppermost ~ 6 nm of the film exhibits a porous morphology, in contrast to the denser structure observed in the rest of the layer. For subsequent analysis we consider the two interfaces and the central region sketched in the right panel of FIG. 1a): the TI, encompassing the Pt/Ta₂O₅ interface; the BI corresponding to the Ta₂O₅/TaO₂ interface; and the central C region containing the Ta₂O₅. The TaO_x in the film is amorphous, while the AgNPs are crystalline.

The NPs are not visible in the STEM images. However, the presence of NPs was unambiguously verified by EDS. Line scans of the device with NPs, shown in FIG. 1c), reveal a distinct Ag signal near the Pt/TaO_x interface, which is absent in devices without NPs, as seen in FIG. 1b). An oxygen concentration gradient is observed throughout both layers of the film, ranging from Ta₂O₅ near the top electrode to TaO near the bottom electrode.

To investigate the memristive behavior of the system, Hysteresis Switching Loops (HSLs) were measured. In this procedure, voltage pulses (referred to as writing pulses) are applied in a ramp sequence. The remnant resistance of the device is then measured between successive writing pulses by applying a small reading pulse (0.1 V) and plotted as a function of the writing voltage. Further methodological details are provided in Refs.[18, 38].

HSLs and the corresponding I-V curves (not shown) were acquired for devices with and without AgNPs. Both kinds of devices initially exhibited a low resistance state and no electroforming step was necessary. This could be due to the porous structure [39] shown in FIG. 1a), or to a low density media that creates high mobility paths [40], which can favor the formation of conductive OV filaments through internal surfaces without the need for an electroforming step.

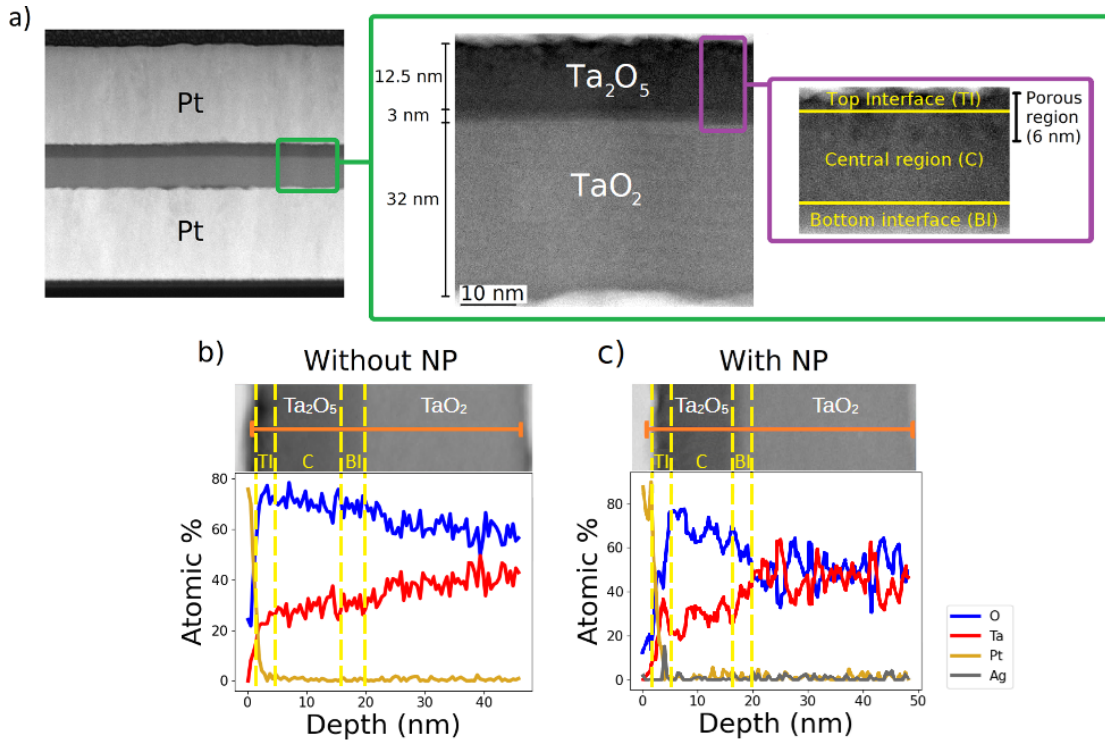


FIG. 1: a) STEM-HAADF cross-sectional image of a device with Ag nanoparticles (AgNPs) embedded in the top electrode. The active zone of the device together with the top, central and bottom interfaces (TI, C and BI respectively) are zoomed in by the green and violet rectangles, respectively. See text for details. EDS linescans of the device taken along the orange line. Ta, O, Pt and Ag species are quantified: b) Without AgNPs, c) With AgNPs.

In devices without AgNPs, the application of a symmetrical voltage ramp produced a "table with legs" (TWL) type of HSL (see FIG. 2a)). By modifying the symmetry of the electrical stimulus, it was possible to isolate two HSLs with opposite circulations: a CCW loop (FIG. 2b)) and a CW loop (FIG. 2c)). The high-resistance (HR) values were around ~ 1.4 - 1.5 k Ω , and slightly different for both, CCW and CW, HSL. On the other hand, the low-resistance (LR) state was essentially the same for both loops and about 120 Ω . Note in addition, that the TWL also exhibits two HR levels, in contrast to the case of symmetric devices for which a single one is obtained

[41, 42]. In Sec. IV we will further elaborate on these results using the OVRN model.

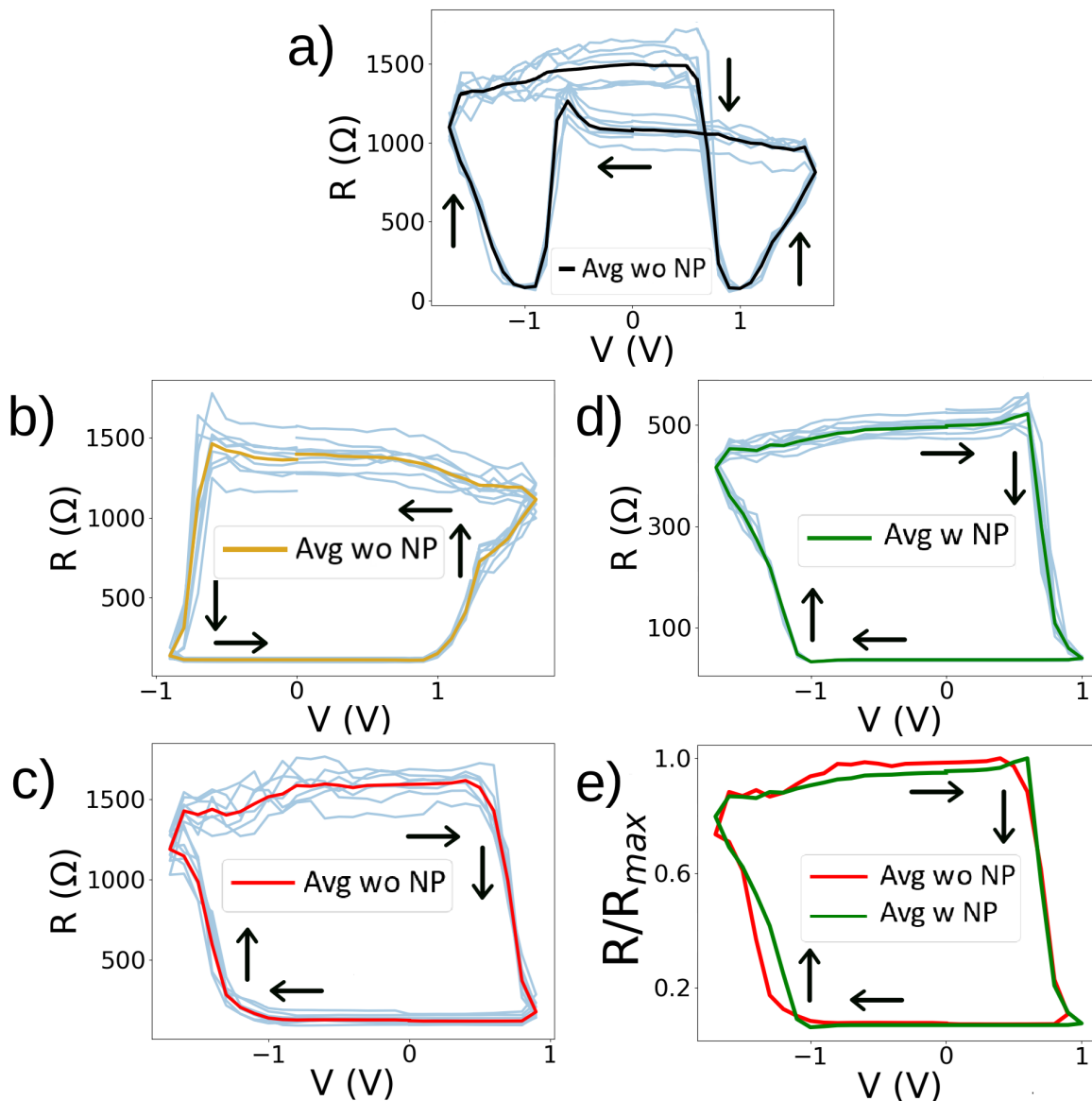


FIG. 2: Electrical characterization of TaO_x devices with (w) and without (wo) Ag nanoparticles (AgNPs). Measured individual hysteresis switching loops (HSL) (light blue lines) and average (Avg) HSL. Arrows indicate the circulation direction. a) Table with legs HSL in a device wo AgNPs. b) Counter-clockwise HSL wo AgNPs. c) Clockwise HSL wo AgNPs. d) Clockwise HSL in a device w AgNPs. e) Clockwise HSL for devices wo and w AgNPs.

The SET and RESET voltages were similar in magnitude across both loops (0.9 V and 1.5 V, respectively), with their polarity reversing according to the loop circulation. However, SET transitions are observed to be relatively abrupt, which is consistent with a FRS mechanism driven by

OV migration.

Devices containing AgNPs exhibited a markedly different behavior as only the CW loop was experimentally obtained (see FIG.2d)). Additionally, the resistance levels were significantly reduced compared to those of devices without NPs, with the HR and LR states roughly of 450Ω and 30Ω respectively. Notice that the SET and RESET transitions take place at the same voltages and have a similar trend than in the CW cycle without NPs. To reinforce these features, the average CW HSLs from both device types were normalized to their maximum resistance values and plotted together in FIG.2 e). The near-perfect overlap of these curves suggests that the underlying RS mechanism remains mostly unchanged regardless of the presence of NPs.

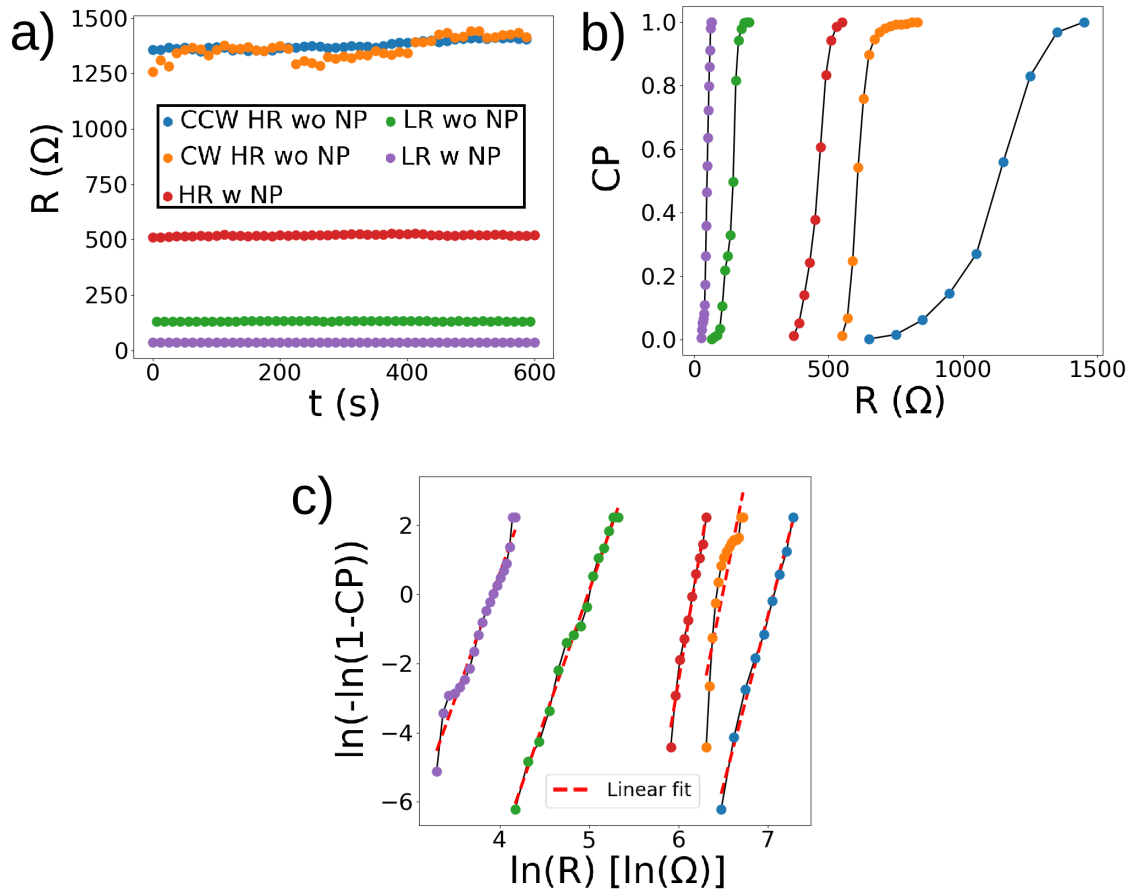


FIG. 3: a) Retentivity test showing all resistive levels. b) Cumulative probability distribution function (CP) obtained as a result of 500 ON/OFF cycles for devices wo and w AgNPs. c) Linear Weibull fittings (dashed lines) of $\ln(-\ln(1-CP))$ vs $\ln(R)$ for each of the resistive levels of devices with and without AgNPs. See text for details.

To further investigate the stability and nature of the RS effect, short-term retention tests were

performed and displayed in FIG. 3a). The resistance states remained stable in both type of devices over 10 minutes, indicating the absence of volatile switching effects regardless of the presence of NPs. To test device durability, 500 ON/OFF cycles were carried out, resulting in a much narrower cumulative probability distribution (CP) for both high and low resistance levels in the case of devices with AgNPs (as seen in FIG. 3b)).

The evolution of both the HR and LR states of a given device upon repeated cycling can be analyzed with the Weibull cumulative probability distribution [43, 44], given by

$$CP_w(R, \lambda, k) = 1 - e^{-\left(\frac{R}{\lambda}\right)^k}, \quad (1)$$

with λ being the scale parameter, k the shape parameter and R the resistance. A typical approach is to use $\ln(-\ln(1 - CP_w)) = k \ln(R) - k \ln(\lambda)$, which displays linear behaviour as a function of $\ln(R)$. In FIG.3c) we used the CP values shown in FIG. 3b) and plot $\ln(-\ln(1 - CP))$ versus $\ln(R)$. After performing a linear fit, we get the k and λ values shown in TAB. 1.

Incorporation of AgNPs improves the cycle-to-cycle uniformity of the HR states, as evidenced by a steeper cumulative probability distribution and a higher shape parameter k , compared to those of the HR states without AgNPs. This evidences that devices with AgNPs present reduced statistical dispersion and enhanced switching reproducibility. This improvement is consistent with the AgNPs-induced local metallization of the top interface, which pins OV configurations and effectively reduces the number of accessible microscopic switching pathways. As a result, the RS dynamics becomes predominantly governed by the bottom interface, yielding steeper Weibull cumulative distributions and more stable endurance.

Resistive level	k	$\lambda(\Omega)$
CCW HR wo AgNP	9.8	7.1
CW HR wo AgNP	12.8	6.4
LR wo AgNP	7.4	4.9
HR w AgNP	15.4	6.2
LR w AgNP	7.3	3.9

TAB. 1: Shape parameter k and scale parameter λ values obtained via Weibull fittings of the resistive levels of devices w and wo AgNPs.

IV. MODELLING

The described electrical response can be explained and modelled in terms of FRS. In this scenario, the LR state is associated to formed OV filaments, while their retraction and regrowth, mainly at the TI and BI-driven by external applied voltage biases of opposite polarities, give rise to the LR \leftrightarrow HR transitions and, therefore, to the RS effect.

In the device without NPs, and depending on the history of the applied voltage, the system can reach three distinct resistive states: a LR state and two high resistance states (HR1 and HR2). The first corresponds to OV filaments fully formed. Meanwhile, the latter ones are related to OV partially expelled from the TI (HR1) and the BI (HR2), with the concomitant break up of the previously formed OV filaments. FIG. 4a) shows a sketch of these processes, that we describe in more detail in what follows: Considering the LR state as the initial state, a positive voltage applied to the top electrode drifts OV (being positively charged defects) towards the bottom electrode. As OV migration takes place predominantly near the interface regions where the Schottky barriers enhance the local electric field, OV filaments are thus expelled from the TI towards the C region, where the OV dynamic is mostly suppressed. In addition, due to the lower resistivity of the BI, the electric field intensity is attenuated there compared to that in the TI (as discussed below), so OV filaments break to a lesser extent or only partially. Altogether this behavior leads to the HR1 state. Afterwards, a negative bias applied to the TE can re-build the OV filaments, leading back to the LR state. This switching between LR and HR1 defines the CCW cycle depicted in FIG. 4a) left.

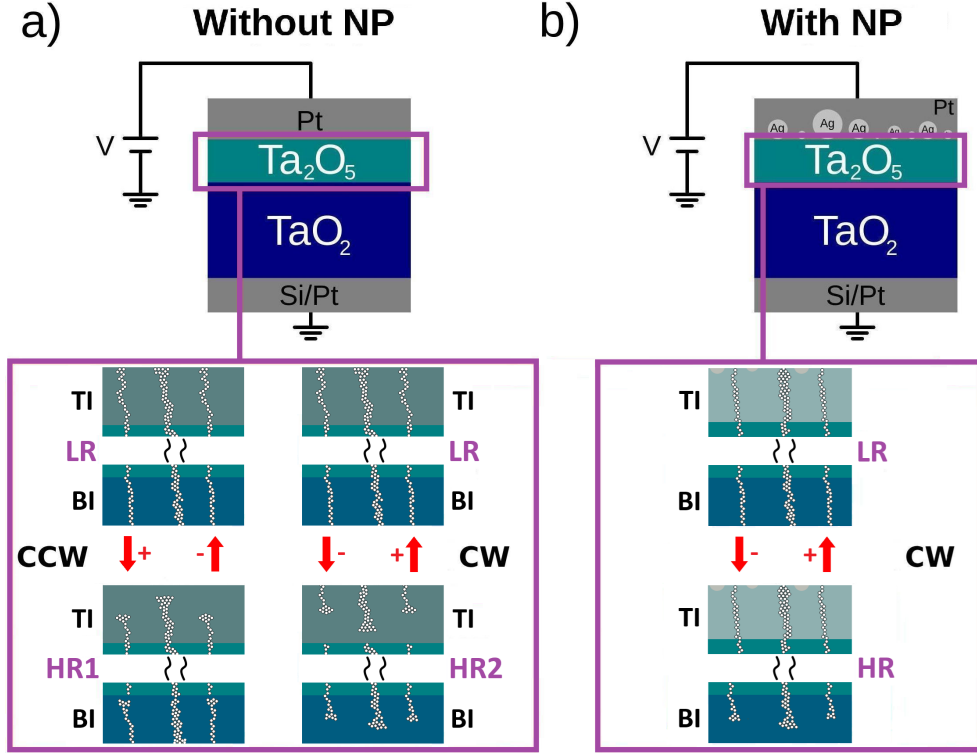


FIG. 4: Scheme of the device with the active region for RS- comprising the TI, C and BI -enclosed by the violet rectangle. a) Without NPs:OV filaments bridge the Ta_2O_5 layer (LR state). When an external stimulus is applied, these filaments retract/grow at the TI/BI interfaces (HR1 and HR2 states). b) With AgNPs: RS is mostly restricted to the BI, giving a single CW cycle. See text for details.

On the other hand, starting from the same LR state, a negative voltage drives OV toward the top electrode and from the BI towards the C region. This process leads to the HR2 shown in FIG. 4a) right. In analogy with the previous description, a subsequent positive bias will re-build or enlarge OV filaments at both interfaces, recovering the LR state. This hole process produces the CW cycle between LR and HR2.

For the present analysis we assume that the LR state is shared by the two cycles—CCW ($\text{HR1} \rightleftharpoons \text{LR}$) and CW ($\text{HR2} \rightleftharpoons \text{LR}$)—allowing access to either HR1 or HR2 depending on the polarity of the applied stimulus. This assumption relies on the experimental measurements that give the same LR states for both CW and CCW HSL (see FIG. 2 b) and c)). In spite of the fact that our numerical simulations support this hypothesis (see below), it would be ideal to have experimental images of OV distributions, which are not accessible with current capabilities.

With the introduction of AgNPs at the top electrode, the TI is metallized in the vicinity of the NPs. This creates low resistivity regions that anchor OV dynamics due to the weak electric field, inhibiting OVs to be expelled towards the C region, thus rendering the HR1 state inaccessible. OV dynamics is (mostly) limited to the BI region (see FIG. 4b)), concomitantly with a single CW HSL, as was obtained in the experiment (FIG. 2 d)).

To validate the proposed response, we perform simulations using the OVRN model [33], which accounts for resistance variations in a resistor network by considering the migration of OV under the influence of an external electrical stimulus. Owing to the dependence of the oxide's local resistivity on its specific oxygen stoichiometry, the model enables a precise description of the evolution of the overall device resistance as OV dynamics takes place. In addition, the 2d nature of the model allows to simulate the filamentary behaviour, successfully reproducing features such as the abnormal SET process observed in TaOx-based devices [45].

The OVRN considers the oxide as a $N \times M$ grid of nanodomains in the x-y plane, each one labelled with an index k ($1 \leq k \leq N \times M$). The resistivity (ρ_k) of a nanodomain is determined by its local OV concentration (δ_k) according to

$$\rho_k = \rho_M - \rho_m \tanh[A(\delta_k - \delta_M)], \quad (2)$$

where $\rho_m = (H\rho - L\rho)/2$ and $\rho_M = (H\rho + L\rho)/2$, with $L\rho$ and $H\rho$ being the maximum and minimum resistivities attainable by a given domain respectively. In the simulations we have considered different values of ρ_m and ρ_M for the TI, C and BI respectively, to take into account the different resistivity ranges of each region (See Table 2 for the parameters' values. The parameter δ_M denotes a threshold vacancy concentration, such that for $\delta_k = \delta_M$ the resistivity of the domain k is ρ_M . The constant A controls the sharpness of the transition between the high (and low) resistivity states. Since OV act as n-type dopants, their accumulation locally reduces the resistivity. The hyperbolic tangent function effectively captures this behavior, while not allowing the resistivity to decrease indefinitely. The first N_{TI} rows were assigned to the TI region, the last N_{BI} rows to the BI region and the remaining sites to the central (C) region. Each simulation step at time t starts with a defined OV profile $\delta_k(t)$, which determines a resistivity profile $\rho_k(t)$. An external voltage $V(t)$ is applied to the top electrode (the bottom electrode remains grounded). Using Kirchhoff's laws, the local voltage drops ΔV_k^l ($l = x$ or $l = y$) across each site are computed along with the total resistance $R(t)$ of the network. The OV migration rates (transition probability per unit time) from

a domain k to its four nearest neighbours k' are obtained through

$$p(k, k') = \delta_k(t)(1 - \delta_{k'}(t)) \exp(-V_\alpha^l + \Delta V_k^l), \quad (3)$$

where V_α^l is the activation energy for OV diffusion, expressed in units of the thermal energy kT . The vacancy profile at time $t + \Delta t$ is then updated to

$$\delta_k(t + \Delta t) = \delta_k(t) + \sum_{k'} (p(k', k) - p(k, k')) \Delta t, \quad (4)$$

and with these values the new resistivity profile $\rho_k(t + \Delta t)$ is obtained.

Using the OVRN model, two sets of simulations were performed, without and with AgNPs, respectively. All simulations were initialized with a randomized OV profile and in accordance with experimental observations, the system was set initially in a low resistance state, corresponding to fully formed OV filaments. A voltage ramp was applied until the HSL stabilized. We consider 100 random generated initial OV configurations and the HSL is obtained by averaging over all the realizations.

In the simulations without NPs, the TI and BI were chosen more resistive than the C region, consistent with the formation of Schottky barriers at both interfaces [18, 34, 35]. Simulated CCW (FIG. 5a) and CW (FIG. 5b) cycles have been properly isolated by stimulating the system with a non-symmetrical voltage ramp. The average experimental HSL were also plot for comparison, showing an excellent agreement with the simulated ones. Likewise, for a symmetrical voltage ramp, the simulated HSL displays a TWL (FIG. 5c)), in quite good agreement with the experimental one. It is worth noting, however, that certain features of the experimentally observed high-resistance states are not reproduced by the simulations. These include, for example, the resistance of the CCW level in the TWL configuration and the upward drift in resistance observed between the RESET and SET processes. Such discrepancies may arise from the presence of slight diffusive processes linked to memristive filamentary mechanisms, triggered by the presence of high oxygen vacancy gradients [46] which are not fully collected by the model.

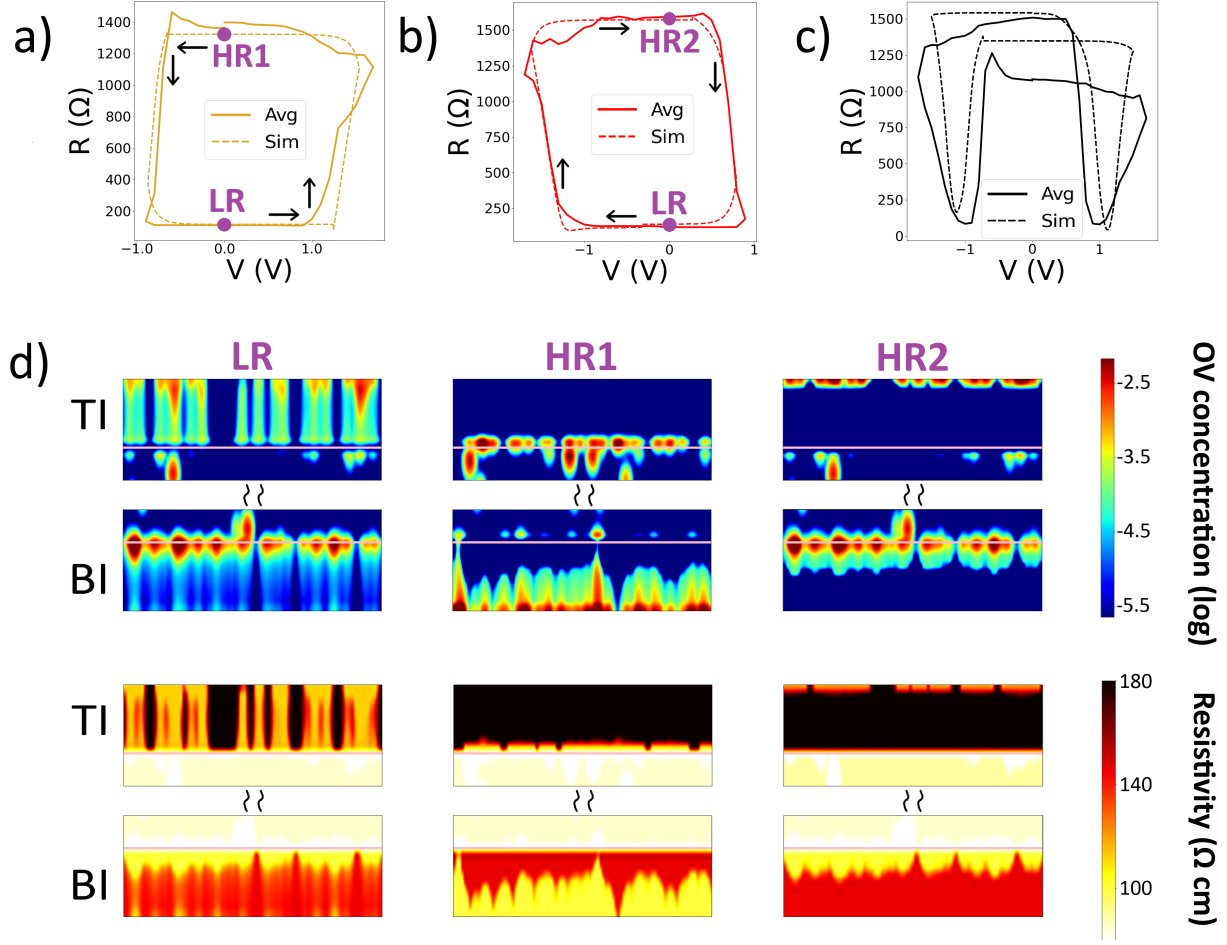


FIG. 5: Top panels: Average experimental (solid lines) and simulated (dashed line) HSLs for the device without NPs. a) TWL, b) CCW and c) CW, HSLs. d) OV concentration (upper panel) and resistivity profiles (bottom panel) near the TI and BI, for the LR (left panels), HR1 (central panels) and HR2 (right panels) resistance states indicated in a) and b).

The OV and resistivity profiles correspondent to the high resistance states, HR1 and HR2, in addition to those of the LR state, are displayed in FIG. 5d). Depending on the polarity of the applied voltage, the OV filaments retract/grow at both the TI and BI. Note that, due to the weak electric field in the C region, the OV distribution there remains largely unchanged; therefore, we show only the OV and resistivity profiles of the C region near the TI and BI, respectively.

Parameter	Numerical value (a.u.)	Value in units
Applied voltage V (abs. value)	0 to 1600	0 V to 1.6 V
A	10^7	200 nm ²
δ_M	$1.4 \cdot 10^{-4}$	0.3 nm ²
KT@RT (300 K)	1	25 meV
V_α (in units of KT)	13	13
N	100	60 μ m
M	100	15 nm
M^{TI}	10	1.5 nm
M^C	80	12 nm
M^{BI}	10	1.5 nm
$\rho_M^{TI} - \rho_m^{TI}$	77 - 32	$5.6 \cdot 10^2 \Omega \cdot m - 2.8 \cdot 10^2 \Omega \cdot m$
$\rho_M^C - \rho_m^C$	28 - 5	$2 \cdot 10^2 \Omega \cdot m - 0.1 \cdot 10^2 \Omega \cdot m$
$\rho_M^{BI} - \rho_m^{BI}$	60 - 22	$4.3 \cdot 10^2 \Omega \cdot m - 1.6 \cdot 10^2 \Omega \cdot m$
$\rho_M^{NP} - \rho_m^{NP}$	41 - 24	$2.9 \cdot 10^2 \Omega \cdot m - 1.7 \cdot 10^2 \Omega \cdot m$

TAB. 2: Parameters used in the OVRN model converted from a.u to physical units. See text for more details.

An interesting outcome that captures the experimental results, is the emergence of distinct HR1 and HR2 values arising, as we have already mentioned, from the different resistivity ranges assumed for the TI and BI. In particular, the resistivity of the BI was taken lower than the TI one -in consistency with the higher metallic content obtained by the EDS scans reported in FIG. 1b)–c). Notice that even for the LR state, the OV concentrations and resistivities profiles are quite different in both interfaces and this affects the subsequent OV dynamics. When a positive stimulus is applied, the attained HR1 state still presents several complete filaments in the BI, while the OV filaments have almost disappeared from the TI. In contrast, in the HR2 state both interfaces exhibit broke up filaments and, as a consequence, the HR2 value results slightly higher than the HR1 one. In addition, we also considered different Schottky barriers for both interfaces. As the BI is formed between two stoichiometries of the same oxide, it is expected to have a lower Schottky barrier than

the Pt/Ta₂O₅ interface. This reduces the local electric field and the OV migration along the BI, in consistency with the described behaviour.

The predominance of the interfaces in controlling OV migration due to the strong electric fields there developed, also stabilizes the electric response, producing a more reliable RS effect than that associated with filament rupture due to Joule heating [17, 47].

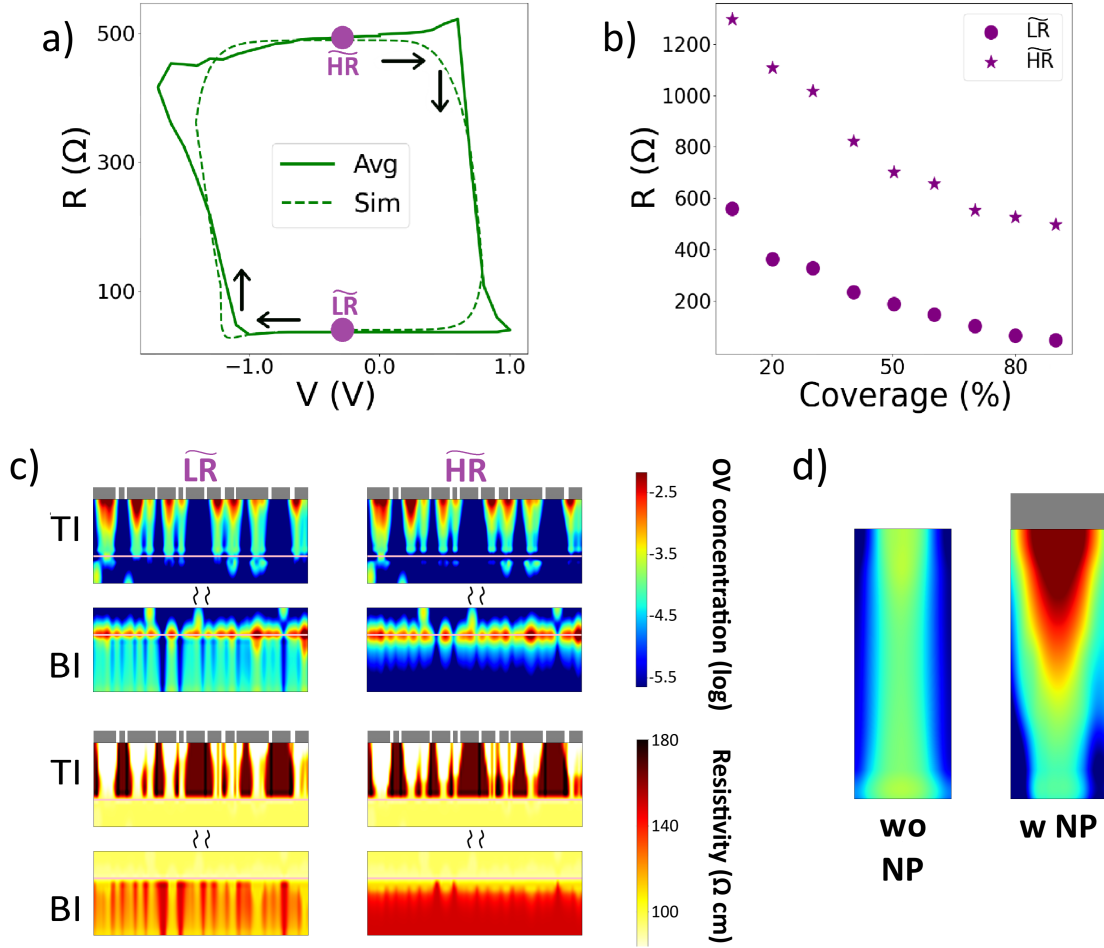


FIG. 6: a) Average experimental (solid line) and simulated (dashed lined) HSL for the system with AgNPs. b) Simulated \widetilde{HR} and \widetilde{LR} levels as a function of the AgNP coverage. Notice that the simulated HSL in a) corresponds to a 80 % of coverage. c) Simulated OV concentration (upper panel) and resistivity profiles near the TI and BI (bottom panel) for the \widetilde{LR} (left) and \widetilde{HR} (right) states indicated in a). The AgNPs positions are sketched by the grey regions above the TI. d) OV filament without (left) and with AgNPs (right).

The effect of incorporating nanoparticles was successfully reproduced using the OVRN model, as is shown by the CW HSL depicted in FIG. 6a). This behaviour was captured in the simulations

by assuming that the TI is locally metallized by the presence of AgNPs. These low resistivity regions have been considered in the simulations by changing properly in Eq. (2) $\rho_M, \rho_m \rightarrow \rho_M^{NP}, \rho_m^{NP}$, in those network sites where NP have been incorporated. Therefore, AgNPs anchor OVs generating persistently a low-resistance state in the TI. Consequently, essentially the BI remains active in the process as is illustrated in FIG. 6c), and therefore the HSL obtained is the CW one. Additionally, the partial short-circuiting of the TI due to the AgNPs lowers the resistance of this region concomitant with the lowering of the overall device resistance, and in agreement with the experimental observations.

The gradual incorporation of AgNPs was simulated and its effect in the overall device resistance shown in FIG. 6b). An 80% coverage in the 2D network simulation, which roughly translates to the 6% measured coverage (see Suppl. Mat. for more details) yields the values measured in the experimental system.

It is interesting to note that the AgNPs have a noticeable effect in OV filament shape, as shown in FIG. 6d). Filaments in the TI of devices with out (wo) NPs tend to be cylindrical in shape, owing to the fact that the electric field caused by the applied electrical stimulus is always strong enough to move the OV along the interface. The anchoring of OVs caused by the AgNPs gives conical shaped filaments, with more OV concentrated near the AgNPs.

V. DISCUSSION AND CONCLUSIONS

In conclusion, we have demonstrated that the incorporation of Ag nanoparticles (AgNPs) into the top electrode of Pt/Ta₂O₅/TaO₂/Pt memristive devices provides an effective means to tailor their resistive switching (RS) behavior. Devices without nanoparticles exhibit two distinct hysteresis switching loops (HSLs) with opposite chiralities, which originate from the participation of two active interfaces—Pt/Ta₂O₅ and Ta₂O₅/TaO₂—and share a common low-resistance state. Introducing AgNPs leads to a significant reduction of the overall device resistance and selectively suppresses one of the switching loops, resulting in a single, well-defined switching mode.

This behavior can be consistently understood within a filamentary RS framework. In the absence of AgNPs, Schottky barriers at both interfaces enhance the local electric field and promote oxygen vacancy (OV) migration, enabling two competing switching channels associated with filament retraction and regrowth at either interface. When AgNPs are incorporated, the top interface becomes locally metallized, partially inhibiting OV transport across this region and effectively

confining the RS dynamics to the bottom interface. As a consequence, only one switching channel remains active.

Although the forming-free behavior of the devices and the presence of AgNPs could, in principle, suggest an electrochemical metallization scenario [40, 48], several observations support an OV-driven filamentary mechanism instead. In particular, forming-free switching was also observed in devices without NPs, no evidence of Ag incorporation within the oxide layer was detected (See Suppl. Mat.), and the interface-selective switching behavior is inconsistent with the formation of metallic Ag filaments.

Beyond the qualitative modification of the switching characteristics, AgNPs incorporation also leads to a marked improvement in endurance stability. Weibull analysis of the cumulative resistance distributions reveals a reduced cycle-to-cycle variability of the high-resistance states in devices with AgNPs compared to their nanoparticle-free counterparts, indicating enhanced switching reproducibility. This increased stability can be attributed to the reduced number of accessible microscopic switching configurations when OV dynamics is confined to a single active interface.

The proposed physical picture is supported by numerical simulations based on the Oxygen Vacancy Resistive Network (OVRN) model, which successfully reproduce the experimental HSLs both with and without AgNPs, as well as the observed reduction in statistical dispersion. The simulations further show that OV filaments predominantly grow and retract at the active interfaces, remaining largely static in the central region, and that the RS characteristics and ON/OFF ratios can be continuously tuned by varying the AgNPs coverage.

More broadly, our findings highlight the potential of NP incorporation as a general strategy to tune memristive behavior across a wide range of transition-metal oxides. Because the mechanism identified here relies on controlling OV dynamics at complementary interfaces, similar approaches can be extended to systems in which multi-interface effects govern resistive switching. The incorporation of metallic nanoparticles can, thus, be used to define or suppress specific switching channels, enabling deliberate control over device performance.

SUPPLEMENTARY MATERIAL

See the supplementary material for details on the STEM-HAADF and EDS study of the sample post-electrical stimulation, together with details on the OVRN model and the calculations performed to estimate the AgNPs coverage in the numerical simulations.

ACKNOWLEDGMENTS

The authors would like to thank the ‘Laboratorio de Microscopías Avanzadas’ at ‘Universidad de Zaragoza’ for providing access to their instruments. We acknowledge the support from EU-H2020-RISE project MELON (Grant No. 872631) and ANPCyT (Grant Nos. PICT2019-0654, PICT2019-02781, and PICT2020A-00415).

-
- [1] A. Sawa, Resistive switching in transition metal oxides, *Materials Today* **11**, 28 (2008).
 - [2] D. Ielmini and R. Waser, *Resistive Switching: From Fundamentals of Nanoionic Redox Processes to Memristive Device Applications* (Wiley-VCH, 2016).
 - [3] W. Banerjee, Q. Liu, and H. Hwang, Engineering of defects in resistive random access memory devices, *Journal of Applied Physics* **127**, 051101 (2020), https://pubs.aip.org/aip/jap/article-pdf/doi/10.1063/1.5136264/19892156/051101_1_1.5136264.pdf.
 - [4] G. S. Kim, H. Song, Y. K. Lee, J. H. Kim, W. Kim, T. H. Park, H. J. Kim, K. Min Kim, and C. S. Hwang, Defect-engineered electroforming-free analog HfO_x memristor and its application to the neural network, *ACS Appl. Mater. Interfaces* **11**, 47063 (2019).
 - [5] G. Tutuncuoglu and A. Mannodi-Kanakkithodi, Role of defects in resistive switching dynamics of memristors, *MRS Communications* **12**, 531 (2022).
 - [6] Q. Wu, W. Banerjee, J. Cao, Z. Ji, L. Li, and M. Liu, Improvement of durability and switching speed by incorporating nanocrystals in the HfO_x based resistive random access memory devices, *Appl. Phys. Lett.* **113**, 023105 (2018).
 - [7] Q. Liu, S. Long, H. Lv, W. Wang, J. Niu, Z. Huo, J. Chen, and M. Liu, Controllable growth of nanoscale conductive filaments in solid-electrolyte-based ReRAM by using a metal nanocrystal covered bottom electrode, *ACS Nano* **4**, 6162 (2010).
 - [8] W. Banerjee, S. Maikap, C. Lai, Y. Chen, T. Tien, H. Lee, W. Chen, F. T. Chen, M. Kao, M. Tsai, and J. Yang, Formation polarity dependent improved resistive switching memory characteristics using nanoscale (1.3 nm) core-shell IrO_x nano-dots, *Nanoscale Res. Lett.* **7**, 194 (2012).
 - [9] B. J. Choi, A. C. Torrezan, K. J. Norris, F. Miao, J. P. Strachan, M.-X. Zhang, D. Ohlberg, N. P. Kobayashi, J. J. Yang, and R. S. Williams, Electrical performance and scalability of Pt dispersed SiO₂ nanometallic resistance switch, *Nano Lett.* **13**, 3213 (2013).

- [10] S. K. Nandi, S. K. Nath, A. E. El-Helou, S. Li, T. Ratcliff, M. Uenuma, P. E. Raad, and R. G. Elliman, Electric field- and current-induced electroforming modes in NbO_x , *ACS Appl. Mater. Interfaces* **12**, 8422 (2020).
- [11] N. Ghenzi, M. J. Sánchez, M. J. Rozenberg, P. Stoliar, F. G. Marlasca, D. Rubi, and P. Levy, Optimization of resistive switching performance of metal-manganite oxide interfaces by a multipulse protocol, *Journal of Applied Physics* **111**, 084512 (2012).
- [12] J. Y. Son and Y.-H. Shin, Direct observation of conducting filaments on resistive switching of NiO thin films, *Applied Physics Letters* **92**, 222106 (2008).
- [13] V. Álvarez Martínez, R. Ramos, V. Leborán, A. Sarantopoulos, R. Dittmann, and F. Rivadulla, Interfacial thermal resistive switching in (Pt,Cr)/ SrTiO_3 devices, *ACS Applied Materials & Interfaces* **16**, 15043 (2024).
- [14] K. Bao, J. Meng, J. D. Poplawsky, and M. Skowronski, Electrical conductivity of TaO_x as function of composition and temperature, *Journal of Non-Crystalline Solids* **617**, 122495 (2023).
- [15] Y. Lu, Y. Matsuda, K. Sagara, L. Hao, T. Otomitsu, and H. Yoshida, Fabrication and thermoelectric properties of Magnéli phases by adding Ti into TiO_2 (2012) pp. 1291–1296.
- [16] A. F. Arif, R. Balgis, T. Ogi, F. Iskandar, A. Kinoshita, K. Nakamura, and K. Okuyama, Highly conductive nano-sized Magnéli phases titanium oxide (TiO_x), *Scientific Reports* **7**, 3646 (2017).
- [17] G. Sassine, S. La Barbera, N. Najjari, M. Minvielle, C. Dubourdieu, and F. Alibart, Interfacial versus filamentary resistive switching in TiO_2 and HfO_2 devices, *Journal of Vacuum Science & Technology B, Nanotechnology and Microelectronics: Materials, Processing, Measurement, and Phenomena* **34**, 012202 (2016).
- [18] C. Ferreyra, M. J. Sánchez, M. Aguirre, C. Acha, S. Bengiό, J. Lecourt, U. Lüders, and D. Rubi, Selective activation of memristive interfaces in TaO_x -based devices by controlling oxygen vacancies dynamics at the nanoscale, *Nanotechnology* **31**, 155204 (2020).
- [19] C. Ferreyra, R. Leal Martir, D. Rubi, and M. J. Sánchez, Oxygen vacancies kinetics in $\text{TaO}_{2-h}/\text{TaO}_{5-x}$ memristive interfaces, *Journal of Physics D: Applied Physics* **57**, 495307 (2024).
- [20] R. Waser and M. Aono, Nanoionics-based resistive switching memories, in *Nanoscience And Technology: A Collection of Reviews from Nature Journals* (World Scientific, 2010) pp. 158–165.
- [21] Y. C. Bae, A. R. Lee, J. B. Lee, J. H. Koo, K. C. Kwon, J. G. Park, H. S. Im, and J. P. Hong, Oxygen ion drift-induced complementary resistive switching in homo $\text{TiO}_x/\text{TiO}_y/\text{TiO}_x$ and hetero $\text{TiO}_x/\text{TiON}/\text{TiO}_x$ triple multilayer frameworks, *Advanced functional materials* **22**, 709 (2012).

- [22] U. Celano, Y. Yin Chen, D. J. Wouters, G. Groeseneken, M. Jurczak, and W. Vandervorst, Filament observation in metal-oxide resistive switching devices, *Applied Physics Letters* **102**, 121602 (2013).
- [23] A. Isaev, O. Permyakova, and A. Rogozhin, Mechanisms of conductive filament formation in hafnium oxide multilayer structures, *Thin Solid Films* **781**, 139993 (2023).
- [24] Y. Yang, P. Sheridan, and W. Lu, Complementary resistive switching in tantalum oxide-based resistive memory devices, *Applied Physics Letters* **100**, 203112 (2012).
- [25] C.-N. Peng, C.-W. Wang, T.-C. Chan, W.-Y. Chang, Y.-C. Wang, H.-W. Tsai, W.-W. Wu, L.-J. Chen, and Y.-L. Chueh, Resistive switching of Au/ZnO/Au resistive memory: an in situ observation of conductive bridge formation, *Nanoscale research letters* **7**, 1 (2012).
- [26] K. Krishnan, T. Tsuruoka, C. Mannequin, and M. Aono, Mechanism for conducting filament growth in self-assembled polymer thin films for redox-based atomic switches, *Advanced Materials* **28**, 640 (2016).
- [27] S. Cheng, M.-H. Lee, X. Li, L. Fratino, F. Tesler, M.-G. Han, J. del Valle, R. C. Dynes, M. J. Rozenberg, I. K. Schuller, and Y. Zhu, Operando characterization of conductive filaments during resistive switching in Mott VO₂, *Proceedings of the National Academy of Sciences* **118**, e2013676118 (2021).
- [28] L. Gao, Y. Li, Q. Li, Z. Song, and F. Ma, Enhanced resistive switching characteristics in Al₂O₃ memory devices by embedded Ag nanoparticles, *Nanotechnology* **28**, 215201 (2017).
- [29] B. Jana, K. Ghosh, and A. Roy Chaudhuri, Mitigation of memory state variability in SiO₂ memristors by Cu nanoparticles incorporation, *Journal of Alloys and Compounds* **1021**, 179690 (2025).
- [30] J. Li, C. Yao, W. Huang, N. Qin, and D. Bao, Highly uniform resistive switching properties of NiFe₂O₄ films by embedding well-ordered pyramid-shaped Pt/Au nanostructures, *Journal of Alloys and Compounds* **890**, 161814 (2022).
- [31] Y. Ning, Y. Lai, J. Wan, S. Cheng, Q. Zheng, and J. Yu, Implementation of synaptic learning rules by TaO_x memristors embedded with silver nanoparticles, *Chinese Physics B* **30**, 047301 (2021).
- [32] R. Goul, A. Marshall, S. Seacat, H. Peelaers, F. C. Robles Hernandez, and J. Z. Wu, Atomic-scale tuning of ultrathin memristors, *Communications Physics* **5**, 260 (2022).
- [33] R. Leal Martir, E. A. Jagla, D. Rubi, and M. J. Sánchez, Oxygen vacancies driven filamentary resistive switching in oxide-based memristive devices, *Journal of Physics D: Applied Physics* **58**, 325306 (2025).
- [34] M. Lee, C. B. Lee, D. Lee, S. R. Lee, M. Chang, J. H. Hur, Y.-B. Kim, C.-J. Kim, D. H. Seo, S. Seo, U.-I. Chung, I.-K. Yoo, and K. Kim, A fast, high-endurance and scalable non-volatile memory device

- made from asymmetric Ta₂O_{5-x}/TaO_{2-x} bilayer structures, *Nature Materials* **10**, 625 (2011).
- [35] V. Y. Zhuo, Y. Jiang, M. H. Li, E. K. Chua, Z. Zhang, J. S. Pan, R. Zhao, L. P. Shi, T. C. Chong, and J. Robertson, Band alignment between Ta₂O₅ and metals for resistive random access memory electrodes engineering, *Applied Physics Letters* **102**, 062106 (2013).
- [36] G. H. ten Brink, G. Krishnan, B. J. Kooi, and G. Palasantzas, Copper nanoparticle formation in a reducing gas environment, *Journal of Applied Physics* **116**, 104302 (2014).
- [37] A. J. T. van der Ree, M. Ahmadi, G. H. Ten Brink, B. J. Kooi, and G. Palasantzas, Stable millivolt range resistive switching in percolating molybdenum nanoparticle networks, *ACS Appl. Mater. Interfaces* **16**, 65157 (2024).
- [38] M. J. Rozenberg, M. J. Sánchez, R. Weht, C. Acha, F. Gomez-Marlasca, and P. Levy, Mechanism for bipolar resistive switching in transition-metal oxides, *Phys. Rev. B* **81**, 115101 (2010).
- [39] B. Chakrabarti, H. Chan, K. Alam, A. Koneru, T. Gage, L. Ocola, R. Divan, D. Rosenmann, A. Khanna, B. Grisafe, T. Sanders, S. Datta, I. Arslan, S. Sankaranarayan, and S. Guha, Nanoporous dielectric resistive memories using sequential infiltration synthesis, *ACS Nano* **15**, 4155 (2021).
- [40] T. Tsuruoka, I. Valov, S. Tappertzhofen, J. van den Hurk, T. Hasegawa, R. Waser, and M. Aono, Redox reactions at Cu,Ag/Ta₂O₂ interfaces and the effects of Ta₂O film density on the forming process in atomic switch structures, *Advanced Functional Materials* **25**, 6374 (2015).
- [41] A. Ignatiev, N. Wu, X. Chen, Y. Nian, C. Papagianni, S. Liu, and J. Strozier, Resistance switching in oxide thin films, *Phase Transitions* **81**, 791 (2008).
- [42] N. Ge, M. Zhang, L. Zhang, J. J. Yang, Z. Li, and R. S. Williams, Electrode-material dependent switching in ta₂o_x memristors, *Semiconductor Science and Technology* **29**, 104003 (2014).
- [43] D. Jana, S. Samanta, S. Roy, Y. F. Lin, and S. Maikap, Observation of resistive switching memory by reducing device size in a new Cr/CrO_x/TiO_x/TiN structure, *Nano-Micro Letters* **7**, 392 (2015).
- [44] W. Román Acevedo, M. H. Aguirre, and D. Rubi, Electrically-driven control of nanoscale chemical changes in amorphous complex oxide memristive devices, *Nanotechnology* **36**, 105201 (2025).
- [45] T. H. Park, S. J. Song, H. J. Kim, S. G. Kim, S. Chung, B. Y. Kim, K. J. Lee, K. M. Kim, B. J. Choi, and C. S. Hwang, Thickness effect of ultra-thin Ta₂O₅ resistance switching layer in 28 nm-diameter memory cell, *Scientific Reports* **5**, 15965 (2015).
- [46] K. Zhang, Y. Ren, P. Ganesh, and Y. Cao, Effect of electrode and oxide properties on the filament kinetics during electroforming in metal-oxide-based memories, *npj Computational Materials* **8**, 76 (2022).

- [47] Y. B. Zhu, K. Zheng, X. Wu, and L. K. Ang, Enhanced stability of filament-type resistive switching by interface engineering, *Sci. Rep.* **7**, 43664 (2017).
- [48] S. Mukherjee, M. M. Ganaie, A. Chatterjee, A. Kumar, S. Sahu, M. Saliba, and M. Kumar, Self-contained analog switching in AgHfO_{3-x} memristor with lattice-sourced Ag filament for reliable synaptic behavior and associative learning, *Small* **21**, e05032 (2025).